Advances in Geo-Energy Research

Vol. 8, No. 2, p. 126-135, 2023

Original article

Experimental and numerical modeling of deformation-cracking mechanics of 3D-printed rock samples with single fracture

Rui Song[1,2], Jun Tian[1]*, Mingyang Wu[2], Jianjun Liu[2]

[1]*School of Geoscience and Technology, Southwest Petroleum University, Chengdu 610500, P. R. China*

[2]*State Key Laboratory of Geomechanics and Geotechnical Engineering, Institute of Rock and Soil Mechanics, Chinese Academy of Sciences, Wuhan 430071, P. R. China*

Keywords:
3D-printed rock
uniaxial compression
extended finite element method
deformation-cracking mechanics

Cited as:
Song, R., Tian, J., Wu, M., Liu, J. Experimental and numerical modeling of deformation-cracking mechanics of 3D-printed rock samples with single fracture. Advances in Geo-Energy Research, 2023, 8(2): 126-135.
https://doi.org/10.46690/ager.2023.05.06

Abstract:
The analysis of mechanical response and deformation-cracking behavior contributes to the high-efficiency extraction of geo-energy and long-term safety of underground engineering structures. Compared to natural cores, the mechanical properties of 3D-printed samples made from quartz sand as raw material are relatively homogeneous, and can be used for quantitative studies on the influence of natural defects on the mechanical properties of rocks. In this work, 3D-printed samples with single fractures of different crack angles, lengths and widths were fabricated and used for uniaxial compression tests. Adopting the digital image correlation method, the stress-strain distribution during uniaxial compression tests were visualized, and the influence of prefabricated fracture characteristics (dip angle, length, and width) on the deformation-failure process were studied. An extended finite element method subroutine for ABAQUS® software was modeled and used for the uniaxial compression simulation, which was validated by experiments. Then, the influence of mechanical parameters (Young's modulus, Poisson's ratio, cohesion, and internal friction angle) on the deformation-cracking mechanics were simulated and studied. The results indicate that, compared to the intact sample, fractures reduce the sample strength. With the extension of fracture length and width, or the decline of fracture angle, both the peak strain and strength of the 3D-printed samples decrease. The splitting tensile failure, or shear failure, or both were determined for the 3D-printed samples with different fracture angles. For the same axial strain, the extension length of the new crack increases linearly with rising Young's modulus and decreases linearly with increasing Poisson's ratio. The initial strain of new cracks decreases linearly with increasing Young's modulus, while little variations are found in samples with different Poisson's ratio. For the same axial displacement load, the peak stress increases linearly with growing internal friction angle and cohesion.

1. Introduction

Natural rock mass is a kind of strongly heterogeneous porous medium with multi-scale complex structure and disordered initial defects (Yang and Liu, 2021; Ishola et al., 2022). A deep understanding of the mechanical response and deformation-cracking behavior contributes to the high-efficiency extraction of geo-energy and long-term safety of underground engineering projects (Pardoen et al., 2020; He et al., 2021; Song et al., 2022). Many scholars have performed hydraulic cutting and wire cutting to fabricate initial defects in natural rocks (e.g., sandstone, marble etc.) for laboratory mechanical tests. They studied the effects of the number of prefabricated fractures (e.g., single fracture, double fractures, multiple fractures) and the fracture morphology (e.g., angle, length, spacing, and filling materials of the fractures) on the mechanical properties and the deformation-cracking response of the rock samples using uniaxial compression test, conventional triaxial compression test, Brazilian disk test, cyclic loading test, etc. (Haeri et al., 2014; Yang, 2015; Zhuang and Zhou, 2020; Jacobsson et al., 2021; Liang et al., 2021; Rashid

Yandy Scientific Press

*Corresponding author.
E-mail address: rsong@whrsm.ac.cn (R. Song); tianjun19960811@163.com (J. Tian); wmyfrac@163.com (M. Wu); jjliu@whrsm.ac.cn (J. Liu).

Received April 7, 2023; revised April 26, 2023; accepted May 12, 2023; available online May 15, 2023.

et al., 2023). The results confirmed that the initial detects reduced the strength of rock samples, and the weakening degree was affected by the geometrical parameters of the fractures. Kallesten et al. (2020) studied the compactness of fractured cores by injecting chemically reactive brine into fractured cores (such as $MgCl_2$ brine) and found that the cracking of the core had a significant impact on the evolution of its porosity and permeability. However, the disordered and heterogeneous pore structure of natural rock adopted in these studies were not controllable, which means it was difficult to avoid the differences in the mechanical properties even if the intact rock samples were assumed to be homogeneous (Lan et al., 2010; Sousa, 2013; Ghasemi et al., 2020; Xu et al., 2020; Abdelaziz et al., 2023).

Three-dimensional printing technology provides a new tool for manufacturing rock-like samples with controllable internal structure, which possess mechanical similarity to natural rock in the intact 3D-printed state and can be regarded as relatively homogeneous (Ju et al., 2014; Jiang et al., 2016; Zhou and Zhu, 2017; Gao et al., 2021; Song et al., 2021). Wang et al. (2018) manufactured 3D-printed fracture network models with different geometric shapes and adopted them for uniaxial compression tests. Sharafisafa et al. (2018) tested the mechanical response of 3D-printed samples with fractures filled by different materials, and used the digital image correlation method to monitor the stress-strain distribution on the sample surface. The results showed that the strength of samples was increased by the filling materials, whose mechanical properties had a great influence on the deformation and failure behavior of samples (Sharafisafa et al., 2021). Song et al. (2020) investigated the mechanical behavior, microstructure and transport characteristics of 3D-printed samples made by silica sand, gypsum powder and coated silica beads under uniaxial and triaxial compression conditions. They found that the coated silica beads and silica sand samples were suitable for simulating highly permeable sedimentary rocks, while the gypsum powder samples were suitable for simulating high stress in soft rocks. However, the properties related to mineral composition were not considered. Since the strength of 3D-printed samples used in these studies was weak, many scholars have attempted to optimize the 3D printing process to enhance the mechanical properties of fabricated samples. Fereshtenejad and Song (2016) explored the effects of printing direction, printing layer thickness, binder saturation and heating process on the strength and mechanical behavior of 3D-printed samples, and put forward the optimal printing scheme of powder 3D printer. Hodder et al. (2018) studied the uniaxial compression strength of 3D-printed samples fabricated by different kinds of binder, and found that increasing the binder usage could enhance the sample strength. Gell et al. (2019) found that curing treatment can effectively improve the strength and brittleness of 3D-printed samples fabricated by artificial gypsum materials, polylactic acid and sandstone materials.

The strength of 3D-printed samples is still much lower than that of natural rocks, which are usually compacted under long-term geological evolutionary processes, achieving high density and cementation between internal mineral particles and leading to strong bonding strength and high mechanical strength. In contrast, 3D-printed rocks are formed by cementing matrix materials using a binding agent, resulting in lower density and weaker bonding strength between material particles, yielding lower mechanical strength. Nonetheless, experimental results based on 3D-printed samples can provide a new validating tool to numerically modeling on the mechanical behavior of natural rocks. Currently, the numerical simulation methods commonly used in rock mass mechanical response include the discrete element method (Ju and Xing, 2022), boundary element method (Ke et al., 2009), conventional finite element method (Wu et al., 2020b), joint finite-discrete element method (Wu et al., 2020a), and extended finite element method (XFEM) (Riazi et al., 2023). The discrete element method is suitable for irregular geometries of cracks and nonlinear behavior but is computationally complex and time-consuming (Haeri et al., 2018). The boundary element method is suitable for smooth cracks and features high computational efficiency, but can neither handle complex deformation behaviors such as crack opening or sliding, nor nonlinear and irregular problems (Ke et al., 2009). The conventional finite element method uses the Lagrange continuous function as a shape function to deal with the fracture propagation problem, which requires the material properties in the element to be continuous, making it suitable for various complex crack shapes. On the other hand, it requires high-precision meshing, has low in computational efficiency and is not suitable for large-scale computation (Wu et al., 2020b). The joint finite-discrete element method is applicable for cracking scenarios considering rock fissures, and homogeneous and heterogeneous rock masses; however, it is computationally complex and time-consuming, and is difficult to apply for the modeling and simulation of crack intersections and complex crack structures (Wu et al., 2020a). Meanwhile, the XFEM was emphasized by many scholars owing to its advantages of handling the fracture propagation without remeshing and the ability of high-efficiency calculation. The XFEM has been applied for the behavior simulation of rock with randomly distributed strength and stiffness (Pakzad et al., 2020), as well as the interaction between hydraulic fractures and natural fractures in multi-scale reservoir formations under confining pressure (Shi et al., 2015; Wang, 2015; Cruz et al., 2018). However, most mechanical parameters used in previous studies, such as Young's modulus, Poisson's ratio, porosity, permeability, and friction coefficient between the crack surfaces, were based on hypothetical or indoor test results, which makes it difficult to overcome the uncertainty of mechanical properties caused by heterogeneity.

In this paper, we conducted experiments and numerical modeling of deformation-cracking mechanics of 3D-printed rock samples with single fracture. The 3D-printed samples with single fractures of different shapes were fabricated and used for uniaxial compression tests. The stress-strain distribution during the uniaxial compression tests were visualized by adopting the digital image correlation method, and the influence of prefabricated fracture geometrical characteristics (fracture dip angle, fracture length and fracture width) on the deformation-failure process and the propagation of new fractures were studied. The XFEM subroutine for ABAQUS® software was modeled and used for the uniaxial compression

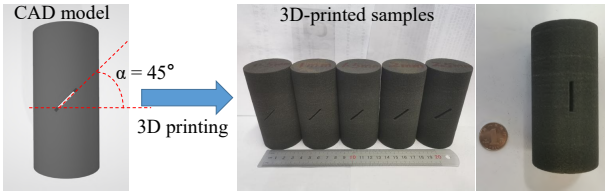

Fig. 1. Schematic diagram of 3D printing process.

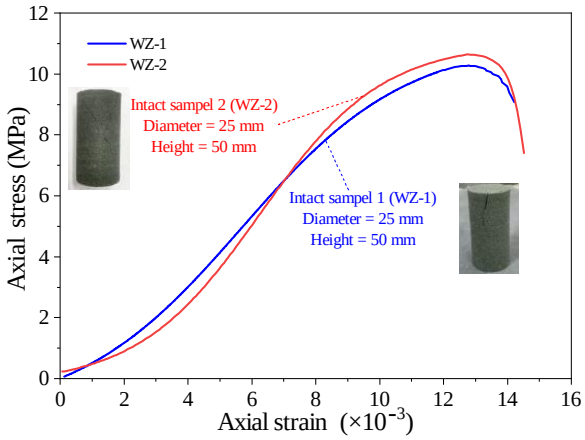

Fig. 2. Stress-strain curve of the two intact samples in the uniaxial compression test.

simulation, and validated by experiments. Then, the influence of physical and mechanical parameters (Young's modulus, Poisson's ratio, cohesion and internal friction angle) on the deformation-cracking mechanics of rock samples were simulated and studied.

2. Materials and Methods

2.1 Sample preparation

Coated quartz sands of spherical shape were selected as the raw material of 3D printing in this study, which mainly contained 95%∼99% quartz sand and 1%∼5% resin. The inkjet printing 3D printer of VX2000 was adopted. The maximum printing accuracy could achieve 0.5 mm, and the maximum size of the 3D-printed samples was 2000 mm × 1000 mm × 1000 mm. Fig. 1 shows the 3D printing workflow, which included (1) the establishment of CAD model of the sample with different fractures (the fracture angle of this model is 45°); (2) transferring the model into STL format file and to the 3D printer; (3) the printer adds the granular materials layer by layer from bottom to top. The 3D-printed samples were designed as a standard cylinder of 50 mm in diameter and 100 mm in height. To mark and monitor the deformation of the 3D-printed samples using the digital image correlation method, the sample surface was coated with spray paint. A layer of white paint on the surface of the sample was firstly applied, and after the white paint dried, the sample was sprayed with fine mist-like black paint particles.

Table 1. Mechanical parameters of the intact sample.

Diameter (mm)	Height (mm)	Young's modulus (MPa)	Compressive strength (MPa)	Peak axial strain ($\times 10^{-3}$)
24.86	50.06	1,186	10.3	12.791

2.2 Experimental setup and procedure

The uniaxial compression tests on the 3D-printed samples were conducted using a microcomputer-controlled electro-hydraulic servo system with the digital image correlation method setup of ARAMIS, which was equipped with a maximum loading of 1,000 kN and a maximum resolution of 0.01% of the measurement accuracy in strain monitoring. The high-resolution images of the strain distribution and the fracture propagation on the surface of the 3D-printed samples were monitored by a high-speed camera. The displacement and strain of the sample surface were calculated by generating the coordinate values of lattice sheets at each stage.

Three groups of 3D-printed samples were manufactured: (1) The fracture length and width of samples in group #1 were 20 and 2 mm, respectively, and the angle varied from 0° to 75°. (2) The fracture angle and width of samples in group #2 were 45° and 2 mm, and the length varied from 5 to 20 mm. (3) The fracture angle and length of samples in group #3 were 45° and 20 mm, and the width varied from 0.5 to 2.5 mm. Loading at the uniform speed of 100 N/s was adopted in the uniaxial compression test, while the fracture propagation was imaged at the frequency of 1 piece/s.

3. Experimental results

In order to study the deformation process of 3D-printed samples, unconfined uniaxial compression tests were carried out on intact samples and samples with different prefabricated fractures. Uniaxial compression tests on intact samples made from the same batch under the same conditions were conducted to test the replicability of the results. The two sets of results show good consistency in terms of the curve growth trend, peak stress and peak strain, as presented in Fig. 2. The average values of mechanical parameters in the laboratory test results of two intact samples are listed in Table 1. Figs. 3(a)-3(c) show that the stress drops rapidly after reaching the peak value, which may be caused by the brittleness of rock. Meanwhile, we observed that the sample was accompanied by surface peeling during the failure process, and a strong failure sound was emitted. When the sample is damaged, it shows typical axial failure characteristics. The above phenomena are similar to the common failure phenomena of natural rock, which indicates the reliability of the 3D-printed samples fabricated in this paper.

It can be seen that the ultimate compressive strength σ_c and axial peak strain ε are lower than those of the intact sample shown in Fig. 3, which is caused by prefabricated fractures. When the angle is 0°, the minimum compressive strength is 2.8 MPa, and the minimum peak strain is 5.925×10^{-3}. Compared with the intact sample, the strength and peak strain are reduced

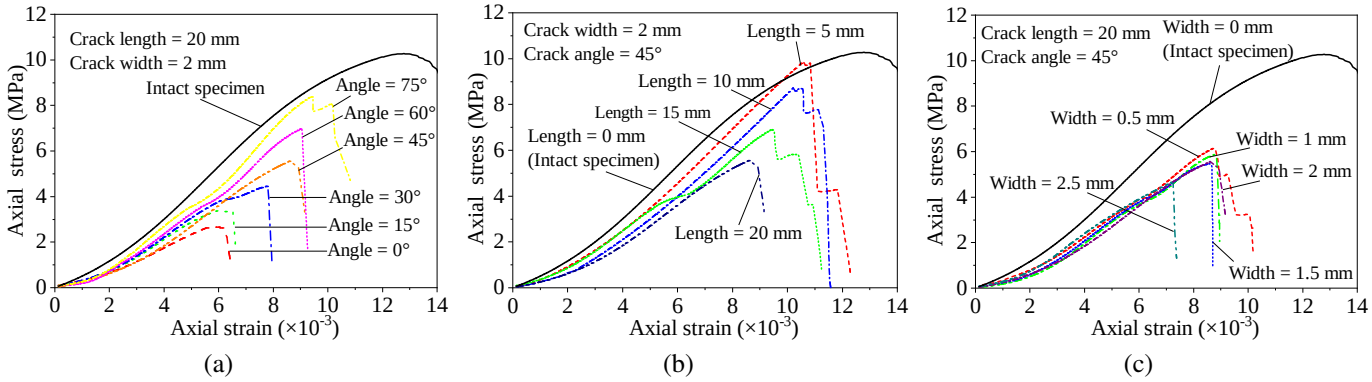

Fig. 3. Stress-strain curves of 3D-printed samples with different (a) angels, (b) lengths and (c) widths.

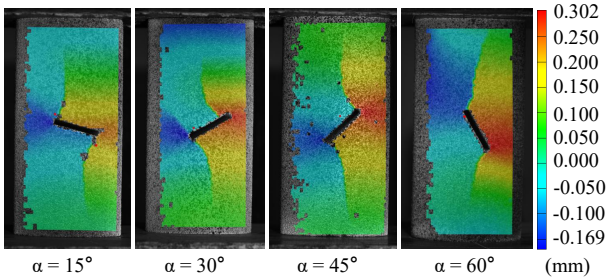

Fig. 4. Horizontal displacement fields of 3D-printed samples with different fracture angles at the failure stage.

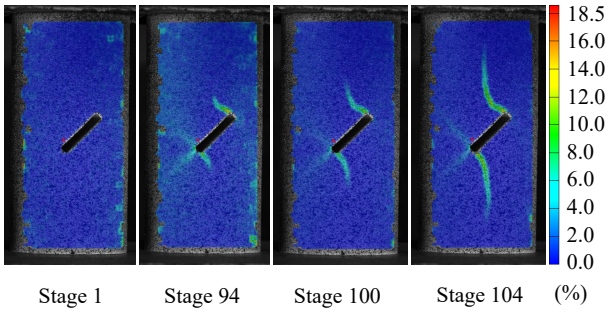

Fig. 5. Strain field evolution of 3D-printed samples (2b=2.5 mm).

by 72.8% and 53.7%, respectively; when the angle is 75°, the maximum compressive strength is 8.4 MPa, and the minimum peak strain is 9.452×10^{-3}. Compared with the intact sample, the strength and peak strain are reduced by 18.4% and 26.1%, respectively. In addition, when the fracture angle increases, the ultimate compressive strength σ_c and axial peak strain ε increase. The above phenomenon indicates that the dip angle of natural fractures has a significant impact on the mechanical properties.

The uniaxial compressive strength σ_c and axial peak strain ε of 3D-printed samples are lower than those of the intact sample, as displayed in Fig. 4. Meanwhile, with the increase in the fracture length 2a (extension length of the crack), the uniaxial compressive strength σ_c and axial peak strain ε decrease. When the length of 2a is 5 mm, the maximum compressive strength is 9.9 MPa, and the maximum peak strain is 10.589×10^{-3}. Compared with the intact sample, the strength is reduced by 3.9%, and the peak strain is reduced by 17.2%; when the length of 2a is 20 mm, the minimum compressive strength is 5.6 MPa and the minimum peak strain is 9.113×10^{-3}. Compared with the intact sample, the strength and peak strain are reduced by 45.6% and 28.8%, respectively.

Fig. 5 shows the phenomenon that, with the increase in the fracture width 2b (distance between the two surfaces of the crack), the uniaxial compressive strength σ_c and axial peak strain ε decrease. This result indicates that the longer the fracture width in the rock, the more easily the rock will be subject to large deformation and failure. In quantitative terms, when the width 2b is 0.5 mm, the maximum compressive strength is 6.2 MPa and the maximum peak strain is 8.863×10^{-3}. Compared with the intact sample, the strength is reduced by 39.8% and the peak strain is reduced by 30.7%; when the width 2b is 2.5 mm, the minimum compressive strength is 4.7 MPa and the minimum peak strain is 7.185×10^{-3}. Compared with the intact sample, the strength is reduced by 54.4% and the peak strain is reduced by 43.8%.

The strength of 3D-printed samples with prefabricated fractures is significantly lower than that of the intact sample, as displayed in Figs. 3(a)-3(c). Meanwhile, similar to the intact sample, the axial stress-strain curves of 3D-printed samples with prefabricated fractures are characterized by four stages: pore compaction, elastic deformation, yield, and strain softening. In the stage of pore compaction, the stress is low and the slope is flat. This phenomenon may be due to the good material homogeneity of 3D-printed samples and the basically consistent initial stiffness. Meanwhile, the nonlinear behavior of concave curve is obvious due to the compression of the internal pores and layer gaps of 3D-printed samples. In the elastic deformation stage, the curves are close to linearity and rise, which may be caused by the volume compression of the structural materials of the sample. In the yield stage, the curve deviates from the linear growth again and becomes less steep. Due to the stress concentration produced by the compression near the prefabricated crack tip of the sample, new cracks begin to initiate and expand along the axial stress direction. In the strain softening stage, the curve declines rapidly after reaching the peak value, because new cracks have propagated and basically penetrated the sample, the sample

is destroyed, and the bearing capacity decreases. The area near the prefabricated fracture tip of each sample presents a large horizontal displacement in the uniaxial compression experiments on the 3D-printed samples, which is shown in Fig. 4. Meanwhile, the horizontal displacement near the left and right tip of the fracture moves in the opposite direction. For the samples with small prefabricated fracture angles (15°, 30°), the horizontal displacement field is symmetrically distributed at the left and right ends of the fracture, showing a tensile failure mode. When the fracture angle is large (60°), the horizontal displacement field is anti-symmetrically distributed near the two tip regions of the fracture, showing shear failure mode. When the fracture angle is 45°, the horizontal displacement field contains both the above two cases. Meanwhile, the failure mode includes both tensile failure and shear failure.

The strain field evolution of 3D-printed samples (2b = 2.5 mm) are shown in Fig. 5. The maximum strain is concentrated at the tip of the prefabricated fracture when the fracture initiates, and an approximately anti-symmetric distribution is formed in the upper and lower regions of the prefabricated fracture. Subsequently, as the load continues to increase, the strain localization band gradually expands along the axial direction of the sample (the upper and lower interfaces of the sample) until it penetrates, which is also the propagation path of the macroscopic fracture. It is worth noting that there are many large strain concentration zones at the tip of the lower left corner of the prefabricated fracture in the samples. This is because the increase in the external load of the sample triggers the deformation of the prefabricated fracture tip area, causing the stress concentration of the surrounding elements. Eventually, damage is caused to the surrounding elements.

4. Numerical modeling and validation

Previous experimental results show that the stress-strain curve of a single-fracture sample obeys the elastoplastic constitutive model and involves the propagation of central cracks. To study the influence of matrix mechanical characteristic parameters of the single-crack sample on its axial strain, crack initiation strain and peak stress, numerical simulation based on XFEM is further carried out in this paper. The detailed simulation theory is described in Section 4.1, and the specific model setup and its validation are included in Section 4.2.

4.1 XFEM theory for numerical simulation

According to the experimental results, the mechanical properties of a single-crack matrix can be described by the Mohr-Coulomb plastic model (Nguyen, 2018), and the fracture propagation behavior is simulated by the XFEM method. The crack propagation process is realized by the traction-separation failure criterion (Lee and Pietruszczak, 2015), which assumes that the constitutive relation of the element is linear elasticity (Zakavi et al., 2022) before the crack appears. Therefore, the relationship between stress and deformation at the interface can be expressed as:

$$t = \begin{Bmatrix} t_n \\ t_s \\ t_t \end{Bmatrix} = K\delta = \begin{bmatrix} K_{mn} & 0 & 0 \\ 0 & K_{ss} & 0 \\ 0 & 0 & K_{tt} \end{bmatrix} \begin{Bmatrix} \delta_n \\ \delta_s \\ \delta_t \end{Bmatrix} \tag{1}$$

where t represents nominal stress (MPa); t_n means normal stress (MPa); t_s and t_t are shear stresses (MPa) in different directions; δ represents the nominal strain; δ_n represents the normal strain; δ_s and δ_t are shear strains in different directions; K represents the strength matrix (K_{ss}, K_{tt} denote shear strength and K_{nn} is normal strength, which are independent of each other, so shear displacement does not cause normal stress change).

When the stress reaches the strength limit, the stress-strain relationship becomes inversely proportional. As the relative displacement of cracks continues to increase, the rock strength begins to degenerate, whereas the stress begins to decrease. When the stress is zero, the rock material is completely damaged. The damage degree of the element is defined by the tension-separation criterion, as follows (Mehraban et al., 2023):

$$\begin{cases} t_n = (1-D)T_n, & T_n \geq 0 \\ t_n = T_n, & T_n < 0 \end{cases} \tag{2}$$

$$t_s = (1-D)T_s \tag{3}$$

$$t_t = (1-D)T_t \tag{4}$$

where T_s, T_t represent the normal stress component (MPa) before damage (linear elastic stage); T_t represents the tangential stress component (MPa) before damage (linear elastic stage); t_n and t_s denote the normal stress component (MPa) after damage occurs; t_t represents the tangential stress component (MPa) after damage occurs; D is the damage variable, which equals 0 when the material is not damaged and equals 1 when the material is completely damaged.

The linear softening model (Yao, 2012) is used to simulate the damage softening behavior in the crack tip region of the sample, and the damage variable D and the separation displacement δ satisfy a certain relationship:

$$D = \frac{\delta_m^f(\delta_m - \delta_m^o)}{\delta_m\left(\delta_m^f - \delta_m^o\right)} \tag{5}$$

where δ_m^f represents the separation displacement (m) when the element is completely damaged; δ_m^o represents the separation displacement (m) when the element begins to be damaged; δ_m denotes the maximum separation displacement (m) in the element failure process.

Considering the combined effect of normal and tangential displacements in the damage process of the element, the separated displacement in the above equation is equivalent to effective displacement:

$$\delta_m = \sqrt{\delta_n^2 + \delta_s^2 + \delta_t^2} \tag{6}$$

In addition, the interface movement is tracked by the level set method (Edke and Chang, 2010):

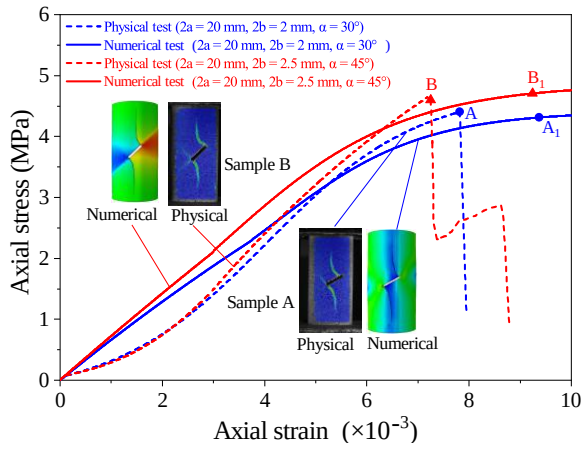

Fig. 6. Comparison results of stress-strain curves in the experiments and simulations.

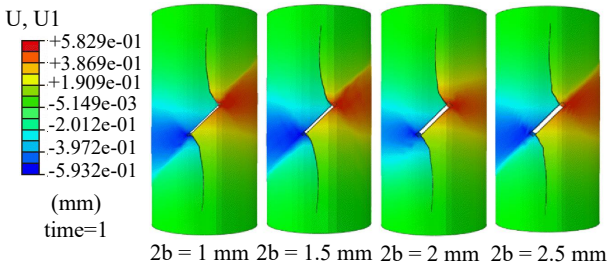

Fig. 7. Horizontal displacement field of 3D-printed samples with different crack widths in the simulation.

$$\varphi(x,t) = \pm \min_{x_c \in \Gamma} ||x - x_c|| \tag{7}$$

Eq. (7) is the level set function of the crack surface, which is used to describe the crack surface, and x_c is any point on the crack surface. The values of Eq. (7) are determined by the relative position of x with respect to the crack defined by Γ, which is positive above the crack and negative below it.

$$\phi_i(x,0) = (x - x_i) \cdot t' \tag{8}$$

Eq. (8) is the level set function of wavefront (Cruz et al., 2019), which is used to describe the position of the crack tip and is orthogonal to Eq. (7) ; t' represents the unit tangential vector at the crack tip, and x_i represents the crack tip.

$$\varphi(x) = \sum_i N_i(x)\varphi_i \tag{9}$$

Eq. (9) can be used to calculate φ at any point x in the region near the crack, and the static geometric interface of the crack can be described as $\varphi(x,0) = 0$, where $N_i(x)$ represents the conventional finite element shape function and φ_i is the node value of the level set function. Both the constitutive model of the sample matrix and the XFEM method of crack propagation simulation can be realized in ABAQUS® software. Therefore, in this paper, the corresponding simulation model is constructed directly by ABAQUS® software.

4.2 Model validation

Standard cylinder samples with a diameter of 50 mm and a height of 100 mm were established. Referring to the constraint situation of previous experiments, the bottom of the model was set as a fixed-end constraint, the site was free and unlimited, and the total displacement load of 1 mm was applied at the top. The initial analysis step was 0.01, and the maximum increment step was 10,000. In addition, three constant parameters were used in the numerical experiments, namely, a failure displacement of 0.001 m, viscosity coefficient of 1×10^{-5}, and friction coefficient of 0.2.

The comparison results of stress-strain curves in the simulation and the experiment are shown in Fig. 6. Obviously, the stress-strain curves obtained by simulation and experiment are in good agreement. In quantitative terms, the axial peak stress and strain of sample A (2a = 20mm, 2b = 2mm, $\alpha = 30°$) are 4.45 MPa and 7.82×10^{-3} in the previous experiment, and they are 4.31 MPa and 9.27×10^{-3} in the simulation, respectively. Meanwhile, the axial peak stress and strain of sample B (2a = 20mm, 2b = 2.5mm, $\alpha = 45°$) are 4.71 MPa and 7.19×10^{-3} in the previous experiment, and they are 4.68 MPa and 9.21×10^{-3} in the simulation, respectively. The above specific quantitative parameters are also close, which confirms the reliability of our simulation models.

It must be noted that the peak strength error between the above experimental and simulation results is less than 5%, but there is a difference in the axial peak strain. The reason is that 3D-printed samples are regarded as ideal homogeneous materials in the simulation. However, real 3D-printed samples may have certain heterogeneity. Taking sample B as an example, in the simulation, when the core sample is compressed by force, the stress increases linearly and stably with the strain. In addition, the sample is regarded as an ideal elastic-plastic body, thus the curve tends to be horizontal after reaching the peak strength point B1. In the experiment, at the initial stage of loading, the pore in the sample and the gap between the layers are compressed and closed, and the elastic modulus is small. Subsequently, the pore compression in the sample gradually reaches the maximum, the layers are in close contact, and the elastic modulus gradually increases and tends to stabilize. When it gets to point B, the curve drops rapidly, showing typical axial splitting failure characteristics. The simulated results for four samples with different crack widths are consistent with the experimental results, which are displayed in Fig. 7. In the laboratory test, the maximum horizontal displacement are +0.3067 and -0.3090 mm (displacement is positive to the right and negative to the left, and the same applies below). In numerical simulations, the maximum horizontal displacement are +0.5829 and -0.5932 mm. However, the field distribution of horizontal displacement in the simulated results is highly symmetrical, and no distortion phenomenon of the horizontal displacement field at the crack tip area can be observed in the experimental results. This is because the specimens in the numerical experiments are considered as completely homogeneous materials, and no collapse or detachment of materials occurred during the compression process.

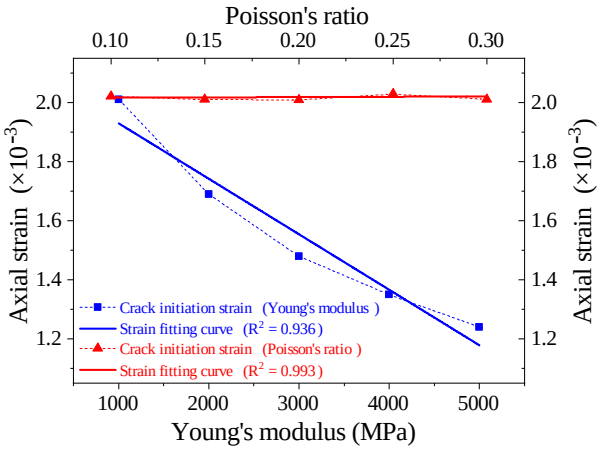

Fig. 8. Relationship between the crack initiation strain and Young's modulus (and Poisson's ratio).

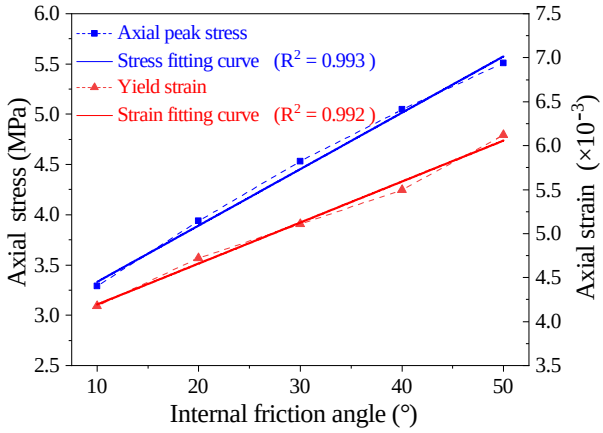

Fig. 9. Relationship between axial peak stress (and yield strain) and internal friction angle.

5. Discussion

5.1 Influence of elasticity parameters

The propagation length of new cracks increases linearly with the enlargement of Young's modulus under the same axial strain. The relationship between axial strain (crack initiation strain) and Young's modulus and Poisson's ratio during crack initiation in numerical simulations are shown in Fig. 8. Apparently, the initiation strain of new cracks in different samples decreases linearly with rising Young's modulus E ($R^2 = 0.936$). In fact, Young's modulus reflects the ability of a material to resist axial deformation and failure. As it gradually increases, the axial stress in the sample increases from small to large under the same axial strain condition. Because the stress threshold required for new cracks in each sample is the same, the crack initiation strain will decrease linearly with increasing Young's modulus. In addition, the crack initiation strain of samples with different Poisson's ratio is about 2.01×10^{-3}, and there is no great difference. Therefore, Poisson's ratio has little influence on the initiation process of new cracks.

5.2 Influence of plastic mechanical parameters

The relationship between the axial peak stress and the internal friction angle in the numerical simulations is presented in Fig. 9. The peak stress increases linearly with rising internal friction angle ($R^2 = 0.993$). This result indicates that increasing the friction angle of the 3D-printed sample matrix can significantly enhance the sample strength. The relationship between axial strain (yield strain) and internal friction angle when the sample yields (from elastic stage to plastic yield stage) in numerical simulations is shown in Fig. 9. The yield strain increases linearly with rising internal friction angle ($R^2 = 0.992$). This phenomenon indicates that the sample with a larger internal friction angle undergoes a longer elastic deformation stage. When the angle of internal friction decreases from 50° to 10° (by 80%), the peak stress decreases from 5.51 to 3.31 MPa (by 39.9%), and the axial strain decreases from 6.1×10^{-3} to 4.2×10^{-3}(by 31.1%).

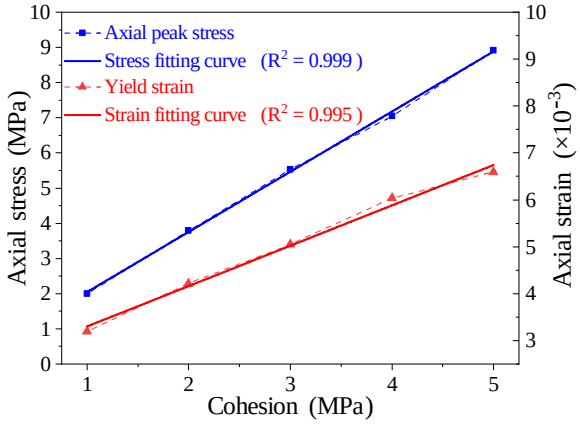

Fig. 10. Relationship between axial peak stress (and yield strain) and cohesion.

The relationship between the axial peak stress and the cohesive force in numerical simulations is displayed in Fig. 10. Basically, the peak stress increases linearly with increasing cohesive force ($R^2 = 0.999$). This indicates that increasing the cohesive force of the 3D-printed sample matrix can significantly enhance the sample strength. The relationship between yield strain and cohesion when the sample has just yielded in numerical simulations is shown in Fig. 10. The yield strain increases linearly with increasing cohesive force ($R^2 = 0.995$), which indicates that the elastic deformation stage of the sample with a higher cohesive force is longer. In addition, when the cohesive force decreases from 5 to 1 MPa (by 80%), the peak stress decreases from 8.92 to 1.94 MPa (by 78.3%), whereas the axial strain decreases from 6.6×10^{-3} to 3.2×10^{-3} (by 51.5%).

6. Conclusions

In this paper, we conducted experiments and numerical modeling on the deformation-cracking mechanics of 3D-printed rock samples with single fracture. Samples with single fractures of different shapes were fabricated by 3D printing and used for uniaxial compression tests. By adopting the

digital image correlation method, the stress-strain distribution during the uniaxial compression tests were visualized, and the influence of prefabricated fracture geometrical characteristics (fracture dip angle, fracture length and fracture width) on the deformation-failure process and the propagation of new fractures were studied. The XFEM subroutine for ABAQUS® software was modeled and used for the uniaxial compression simulation, which was validated by experiments. Finally, the influence of physical and mechanical parameters (Young's modulus, Poisson's ratio, cohesion and internal friction angle) on the deformation-cracking mechanics of rock samples were simulated and studied. The results indicate that:

1) In laboratory tests, compared to the intact sample, fractures reduce the strength of the sample. With increasing fracture length and width, or declining fracture angle, both the peak strain and the strength of the 3D-printed samples decrease. When the fracture angle is 0°, the minimum compressive strength is 2.8 MPa (decreased by 72.8%), and the minimum peak strain is 5.925×10^{-3} (decreased by 53.7%). When the fracture length is 20 mm, the minimum compressive strength is 5.6 MPa (decreased by 45.6%), and the minimum peak strain is 9.113×10^{-3} (decreased by 28.8%). When the fracture width is 2.5 mm, the minimum compressive strength is 4.7 MPa (decreased by 54.4%), and the minimum peak strain is 7.185×10^{-3} (decreased by 43.8%).
2) In laboratory tests, the horizontal displacement in the samples is distributed symmetrically at the ends of the fracture. The splitting tensile failure, or shear failure, or both were determined for the 3D-printed samples with different fracture angles. When the prefabricated fracture angle is 30° or less, the sample presents the characteristics of splitting tensile failure for the 3D-printed samples with the fracture angle of 30° or less, while shear failure is identified for the 3D-printed samples with the fracture angle of 60°. When the fracture angle is 45°, the sample shows both tensile failure and shear failure.
3) In numerical simulations, under the same axial strain, the extension length of the new crack increases linearly with increasing Young's modulus and decreases linearly with increasing Poisson's ratio. The initial strain of new cracks decreases linearly with increasing Young's modulus, while little variations are detected in samples with different Poisson's ratios.
4) In numerical simulations, under the same axial displacement load, the peak stress of the sample increases linearly with rising internal friction angle and cohesion. When the internal friction angle decreases from 50° to 10° (by 80%), the peak stress decreases from 5.51 to 3.31 MPa (decreased by 39.9%), and the yield strain decreases from 6.1×10^{-3} to 4.2×10^{-3} (31.1%). When the cohesive force declines from 5 to 1 MPa (by 80%), the peak stress decreases from 8.92 MPa to 1.94 MPa (by 78.3%), and the yield strain decreases from 6.6×10^{-3} to 3.2×10^{-3} (by 51.5%).

Although the strength of 3D-printed rock is relatively lower compared to natural rock, this study provides a theoretical basis for the constitutive model validation of the deformation-cracking process of rock. In some aspects, the lower strength is beneficial to decreasing the required loading, e.g., to study the cracking process of the rock in the visualized test at the pore scale. Further research will consider the influences of samples with multi-cracks and in-situ loading methods on the deformation and failure processes of rock.

Acknowledgements

This study was financially supported by National Natural Science Foundation of China (No. 51909225) and the Natural Science Foundation of Hubei (No. 2022CFB400).

Conflict of interest

The authors declare no competing interest.

References

Abdelaziz, A., Ha, J., Li, M., et al. Understanding hydraulic fracture mechanisms: From the laboratory to numerical modelling. Advances in Geo-Energy Research, 2023, 7(1): 66-68.

Cruz, F., Roehl, D., do Amaral Vargas Jr, E. An XFEM element to model intersections between hydraulic and natural fractures in porous rocks. International Journal of Rock Mechanics and Mining Sciences, 2018, 112: 385-397.

Cruz, F., Roehl, D., do Amaral Vargas Jr, E. An XFEM implementation in Abaqus to model intersections between fractures in porous rocks. Computers and Geotechnics, 2019, 112: 135-146.

Edke, M. S., Chang, K. H. Shape sensitivity analysis for 2D mixed mode fractures using extended FEM (XFEM) and level set method (LSM)#. Mechanics Based Design of Structures and Machines, 2010, 38(3): 328-347.

Fereshtenejad, S., Song, J. J. Fundamental study on applicability of powder-based 3D printer for physical modeling in rock mechanics. Rock Mechanics and Rock Engineering, 2016, 49(6): 2065-2074.

Gao, Y. T., Wu, T. H., Zhou, Y. Application and prospective of 3D printing in rock mechanics: A review. International Journal of Minerals, Metallurgy and Materials, 2021, 28(1): 1-17.

Gell, E. M., Walley, S. M., Braithwaite, C. H. Review of the validity of the use of artificial specimens for characterizing the mechanical properties of rocks. Rock Mechanics and Rock Engineering, 2019, 52(9): 2949-2961.

Ghasemi, S., Khamehchiyan, M., Taheri, A., et al. Crack evolution in damage stress thresholds in different minerals of granite rock. Rock Mechanics and Rock Engineering, 2020, 53(3): 1163-1178.

Haeri, H., Sarfarazi, V., Zhu, Z., et al. Simulation of crack initiation and propagation in three point bending test using PFC2D. Structural Engineering and Mechanics,

2018, 66(4): 453-463.

Haeri, H., Shahriar, K., Marji, M. F., et al. On the strength and crack propagation process of the pre-cracked rock-like specimens under uniaxial compression. Strength of Materials, 2014, 46(1): 140-152.

He, L., Xiao, H., Cui, Y., et al. Review of visualisation methods of studying the seepage mechanism in fractured rocks. Geomechanics and Geophysics for Geo-Energy and Geo-Resources, 2021, 7(4): 1-25.

Hodder, K. J., Nychka, J. A., Chalaturnyk, R. J. Process limitations of 3D printing model rock. Progress in Additive Manufacturing, 2018, 3(3): 173-182.

Ishola, O., Alexander, A., Vilcáez, J. Statistical and neural network analysis of the relationship between the stochastic nature of pore connectivity and flow properties of heterogeneous rocks. Journal of Natural Gas Science and Engineering, 2022, 105: 104719.

Jacobsson, L., Ivars, D. M., Kasani, H. A., et al. Experimental program on mechanical properties of large rock fractures. Paper Presented at IOP Conference Series: Earth and Environmental Science, Turin, Italy, 20-25 September, 2021.

Jiang, Q., Feng, X., Song, L., et al. Modeling rock specimens through 3D printing: Tentative experiments and prospects. Acta Mechanica Sinica, 2016, 32(1): 101-111.

Ju, Y., Xie, H., Zheng, Z., et al. Visualization of the complex structure and stress field inside rock by means of 3D printing technology. Chinese Science Bulletin, 2014, 59(36): 5354-5365.

Ju, M., Xing, H. Crack propagation in jointed rock and its effect on rock macrofracture resistance: Insights from discrete element analysis. Geomechanics and Geophysics for Geo-Energy and Geo-Resources, 2022, 8(1): 1-22.

Kallesten, E., Andersen, P. Ø., Berawala, D. S., et al. Modeling of permeability and strain evolution in chemical creep compaction experiments with fractured and unfractured chalk cores conducted at reservoir conditions. SPE Journal, 2020, 25(5): 2710-2728.

Ke, C. C., Chen, C. S., Ku, C. Y., et al. Modeling crack propagation path of anisotropic rocks using boundary element method. International Journal for Numerical and Analytical Methods in Geomechanics, 2009, 33(9): 1227-1253.

Lan, H., Martin, C. D., Hu, B. Effect of heterogeneity of brittle rock on micromechanical extensile behavior during compression loading. Journal of Geophysical Research: Solid Earth, 2010, 115: B01202.

Lee, Y. K., Pietruszczak, S. Tensile failure criterion for transversely isotropic rocks. International Journal of Rock Mechanics and Mining Sciences, 2015, 79: 205-215.

Liang, W., Zhao, Y., Liu, J., et al. Advances in in-situ modified mining by fluidization and in unconventional geomechanics. Advances in Geo-Energy Research, 2021, 5(1): 1-4.

Mehraban, M. R., Bahrami, B., Ayatollahi, M. R., et al. A non-local XFEM-based methodology for modeling mixed-mode fracturing of anisotropic rocks. Rock Mechanics and Rock Engineering, 2023, 56(2): 895-909.

Nguyen, T. S. Thermo-Hydro-Mechanical-Chemical processes in geological disposal of radioactive waste - An example of regulatory research. Advances in Geo-Energy Research, 2018, 2(2): 173-189.

Pakzad, R., Wang, S., Sloan, S. W. Three-dimensional finite element simulation of fracture propagation in rock specimens with pre-existing fissure(s) under compression and their strength analysis. International Journal for Numerical and Analytical Methods in Geomechanics, 2020, 44(10): 1472-1494.

Pardoen, B., Bésuelle, P., Dal Pont, S., et al. Accounting for small-scale heterogeneity and variability of clay rock in homogenised numerical micromechanical response and microcracking. Rock Mechanics and Rock Engineering, 2020, 53(6): 2727-2746.

Rashid, F., Hussein, D., Lorinczi, P., et al. The effect of fracturing on permeability in carbonate reservoir rocks. Marine and Petroleum Geology, 2023, 152: 106240.

Riazi, E., Yazdani, M., Afrazi, M. Numerical study of slip distribution at pre-existing crack in rock mass using extended finite element method (XFEM). Iranian Journal of Science and Technology, Transactions of Civil Engineering, 2023, in press, https://doi.org/10.1007/s40996-023-01051-8.

Sharafisafa, M., Aliabadian, Z., Tahmasebinia, F., et al. A comparative study on the crack development in rock-like specimens containing unfilled and filled flaws. Engineering Fracture Mechanics, 2021, 241: 107405.

Sharafisafa, M., Shen, L., Xu, Q. Characterisation of mechanical behaviour of 3D printed rock-like material with digital image correlation. International Journal of Rock Mechanics and Mining Sciences, 2018, 112: 122-138.

Shi, L., Yu, T., Bui, T. Q. Numerical modelling of hydraulic fracturing in rock mass by XFEM. Soil Mechanics and Foundation Engineering, 2015, 52(2): 74-83.

Song, R., Liu, J. J., Yang, C., et al. Study on the multiphase heat and mass transfer mechanism in the dissociation of methane hydrate in reconstructed real-shape porous sediments. Energy, 2022, 254: 124421.

Song, R., Wang, Y., Ishutov, S., et al. A comprehensive experimental study on mechanical behavior, microstructure and transport properties of 3D-printed rock analogs. Rock Mechanics and Rock Engineering, 2020, 53(12): 5745-5765.

Song, R., Wang, Y., Sun, S., et al. Characterization and microfabrication of natural porous rocks: From micro-CT imaging and digital rock modelling to micro-3D-printed rock analogs. Journal of Petroleum Science and Engineering, 2021, 205: 108827.

Sousa, L. M. The influence of the characteristics of quartz and mineral deterioration on the strength of granitic dimensional stones. Environmental Earth Sciences, 2013, 69(4): 1333-1346.

Wang, P., Liu, Y., Zhang, L., et al. Preliminary experimental study on uniaxial compressive properties of 3D printed fractured rock models. Chinese Journal of Rock Mechanics and Engineering, 2018, 37(2): 364-373. (in Chinese)

Wang, H. Numerical modeling of non-planar hydraulic frac-

ture propagation in brittle and ductile rocks using XFEM with cohesive zone method. Journal of Petroleum Science and Engineering, 2015, 135: 127-140.

Wu, Z., Ji, X., Liu, Q., et al. Study of microstructure effect on the nonlinear mechanical behavior and failure process of rock using an image-based-FDEM model. Computers and Geotechnics, 2020a, 121: 103480.

Wu, X., Wang, G., Li, G., et al. Research on shear behavior and crack evolution of symmetrical discontinuous rock joints based on FEM-CZM. Symmetry, 2020b, 12(8): 1314.

Xu, Y., Yao, W., Xia, K. Numerical study on tensile failures of heterogeneous rocks. Journal of Rock Mechanics and Geotechnical Engineering, 2020, 12(1): 50-58.

Yang, S. Strength Failure and Crack Evolution Behavior of Rock Materials Containing Pre-existing Fissures. Beijing, China, Science Press, 2015.

Yang, C., Liu, J. Petroleum rock mechanics: An area worthy of focus in geo-energy research. Advances in Geo-Energy Research, 2021, 5(4): 351-352.

Yao, Y. Linear elastic and cohesive fracture analysis to model hydraulic fracture in brittle and ductile rocks. Rock Mechanics and Rock Engineering, 2012, 45: 375-387.

Zakavi, B., Kotousov, A., Branco, R. Overview of three-dimensional linear-elastic fracture mechanics. International Journal of Fracture, 2022, 234(1): 5-20.

Zhou, T., Zhu, J. An experimental investigation of tensile fracturing behavior of natural and artificial rocks in static and dynamic Brazilian disc tests. Procedia Engineering, 2017, 191: 992-998.

Zhuang, X., Zhou, S. An experimental and numerical study on the influence of filling materials on double-crack propagation. Rock Mechanics and Rock Engineering, 2020, 53(12): 5571-5591.